Environ Sci Pollut Res (2012) 19:3696–3708
DOI 10.1007/s11356-012-0953-6

PHOTOCATALYSIS: FUNDAMENTALS AND APPLICATIONS IN JEP 2011, BORDEAUX

Effect of Nb doping on structural, optical and photocatalytic properties of flame-made TiO_2 nanopowder

Katarzyna A. Michalow · Dorota Flak · Andre Heel ·
Magdalena Parlinska-Wojtan · Mieczyslaw Rekas ·
Thomas Graule

Received: 21 October 2011 / Accepted: 24 April 2012

Abstract TiO_2:Nb nanopowders within a dopant concentration in the range of 0.1–15 at.% were prepared by one-step flame spray synthesis. Effect of niobium doping on structural, optical and photocatalytic properties of titanium dioxide nanopowders was studied. Morphology and structure were investigated by means of Brunauer–Emmett–Teller isotherm, X-ray diffraction and transmission electron microscopy. Diffuse reflectance and the resulting band gap energy were determined by diffuse reflectance spectroscopy. Photocatalytic activity of the investigated nanopowders was revised for the photodecomposition of methylene blue (MB), methyl orange (MO) and 4-chlorophenol under UVA and VIS light irradiation. Commercial TiO_2-P25 nanopowder was used as a reference. The specific surface area of the powders was ranging from 42.9 m^2/g for TiO_2:0.1 at.% Nb to 90.0 m^2/g for TiO_2:15 at.% Nb. TiO_2:Nb particles were nanosized, spherically shaped and polycrystalline. Anatase was the predominant phase in all samples. The anatase-related transition was at 3.31 eV and rutile-related one at 3.14 eV. TiO_2:Nb nanopowders exhibited additional absorption in the visible range. In comparison to TiO_2-P25, improved photocatalytic activity of TiO_2:Nb was observed for the degradation of MB and MO under both UVA and VIS irradiation, where low doping level (Nb<1 at.%) was the most effective. Niobium doping affected structural, optical and photocatalytic properties of TiO_2. Low dopant level enhanced photocatalytic performance under UVA and VIS irradiation. Therefore, TiO_2:Nb (Nb<1 at.%) can be proposed as an efficient selective solar light photocatalyst.

Keywords TiO_2 · Photocatalysis · Visible light · Doping · Niobium · Nanoparticles · Methylene blue · Methyl orange · 4-Chlorophenol

Introduction

Nowadays, domestically and industrially generated waste is an urgent concern, which has to be solved without emission of additional pollutants during waste utilization. Photocatalysis can be a solution. However, there is still a need for an efficient, stable and nontoxic material, which can be activated by solar energy. TiO_2 is still the most common photocatalyst on the market even though it is active only under

Responsible editor: Philippe Garrigues

K. A. Michalow (✉) · D. Flak · T. Graule
Laboratory for High Performance Ceramics, Empa Swiss Federal Laboratories for Materials Science and Technology,
Ueberlandstrasse 129,
8600 Duebendorf, Switzerland
e-mail: katarzyna.michalow@empa.ch

A. Heel
Marketing, Knowledge & Technology Transfer, Empa Swiss Federal Laboratories for Materials Science and Technology,
Ueberlandstrasse 129,
8600 Duebendorf, Switzerland

M. Parlinska-Wojtan
Electron Microscopy Center, Empa Swiss Federal Laboratories for Materials Science and Technology,
Ueberlandstrasse 129,
8600 Duebendorf, Switzerland

D. Flak · M. Rekas
Faculty of Material Science and Ceramics,
AGH University of Science and Technology,
al. Mickiewicza 30,
30-059 Krakow, Poland

M. Parlinska-Wojtan
Institute of Nanotechnology, University of Rzeszow,
ul. Rejtana 16a,
35-959 Rzeszow, Poland

UV irradiation and recombination process is additionally hampering its performance. Therefore, TiO_2 shows poor photocatalytic efficiency under solar irradiation (Fujishima and Zhang 2006; Radecka et al. 2006).

To enhance its efficiency, the light absorption towards the visible range has to be extended, and recombination of the charges has to be minimized. One of the interesting properties of TiO_2 is its susceptibility for structure modification by doping. The cationic sublattice can be doped with either donor-type ions such as W^{6+}, Mo^{6+} or Nb^{5+} (Akurati et al. 2008; Cui et al. 1995; Kubacka et al. 2009; Mattsson et al. 2006; Michalow et al. 2008; Michalow et al. 2009a) or acceptor-type ions such as Cr^{3+} or Fe^{3+} (Borgarello et al. 1982; Radecka et al. 2010; Trenczek-Zajac et al. 2009). The anionic sublattice of TiO_2 can be doped with N, S or F (Asahi et al. 2001; Chen and Mao 2007; Michalow et al. 2009b). However, anionic doping suffers from thermal instability and subsequent ageing problems. Therefore, doping of the cationic sublattice is more reasonable if outdoor applications are considered.

Among donor type of dopants, niobium as a pentavalent ion (Nb^{5+}) with a similar ionic radius (0.69 Å) to that of Ti^{4+} (0.64 Å) seems to be optimal (Shannon 1976). In addition, Nb as Nb_2O_5 can be isotropically dissolved in TiO_2, and a solid solution can be formed for a wide concentration range. Modification by transition metal ion doping is particularly of interest to increase the electrical conductivity and to decrease recombination losses. Finklea (1988) reported a charge carrier density on a level of 10^{19} cm^{-3} for TiO_2:0.1 at.% Nb and location of a unionized donor Nb^{4+} at 0.12 eV below the conduction band, which can act as shallow trapping centres. There are also some contradictions among researchers regarding effect of Nb on the optical properties. A red shift of ~0.15 eV of the fundamental absorption edge was reported for low doping at the level of 0.5 at.% Nb (Wang et al. 1995) and the same effect for high dopant concentration of about 20 at.% Nb (Mattsson et al. 2006). On the other hand, Gautron et al. (1983) reported no band shift for TiO_2-NbO_2 solid-state solution with 20 at.% Nb. Doping by Nb can create stronger acid sites on TiO_2 surface that contributes to the enhancement of catalytic activity and selectivity for various catalytic processes including photocatalytic decomposition (Okazaki and Okuyama 1983; Cui et al. 1995; Akurati et al. 2008). TiO_2:Nb materials are already used for a great variety of applications, e.g. as a gas sensor (Atashbar et al. 1998; Sharma et al. 1998; Carotta et al. 1999; Ferroni et al. 2000; Anukunprasert et al. 2005; Ruiz et al. 2003; Teleki et al. 2008; Traversa et al. 2001; Zakrzewska et al. 1997), as anodes in photoelectrochemical cells for water splitting (Trenczek-Zajac et al. 2007; Wang et al. 1995), as electrodes for dye-sensitized solar cells (Tsvetkov et al. 2011a, b) and seems to be well-performing material for photocatalytic decomposition of organic pollutants under solar irradiation (Mattsson et al. 2006).

Another way to improve a photocatalyst performance is a downscaling of the particle dimension. With nano-size, new physical and chemical properties emerge as well as an increased reactive surface leads to enhanced light absorption and water/hydroxyl groups/pollutant adsorption. It is also known that highly crystalline nano-anatase particles are the most suitable for a photocatalytic application (Almquist and Biswas 2002; Chen and Mao 2007; Sclafani and Herrmann 1996).

The present study reports on the synthesis of TiO_2:Nb anatase-phase nanoparticles by liquid-fed one-step flame spray synthesis (FSS). Employing FSS with acetylene as a flame fuel guaranteed a high temperature (~3,300 K). Therefore, well-crystalline nanoparticles were obtained with high production rate with no need for posttreatment. For as-prepared TiO_2:Nb nanoparticles, an effect of Nb^{5+} dopant on the structural and optical properties of TiO_2 was investigated. The major aim of such a material composition is to increase the spectral sensitivity of the photocatalyst towards the visible light range, which composes the largest part of the solar irradiation and therefore the development of an efficient and pollution-free waterwaste remediation system.

Experimental

Synthesis of Nb-doped TiO_2 nanoparticles

TiO_2:Nb nanopowders with a dopant concentration in the range of 0–15 at.% were prepared by a one-step FSS using titanium tetraisopropoxide (TTIP; $Ti(C_3H_7O)_4$ 99 %, VWR International) and a solution of niobium chloride ($NbCl_5$; 99 %, ABCR) in ethanol (99 %, Sigma Aldrich). Details of the flame spray setup are reported elsewhere (Akurati et al. 2008; Michalow et al. 2008). The required composition of the produced particles was obtained by adjusting a proper ratio of the feed flow rates of the TiO_2 precursor TTIP (FR_{TTIP}) and the dopant precursor (FR_D). TiO_2 precursor and dopant precursor were fed individually by using two syringe pumps. The process control parameter λ_{FSS} (oxygen-to-fuel ratio in the FSS combustion process) was kept constant for all syntheses. The total flow rate of the precursor mixture was in the range of 0.135–0.155 cm^3 s^{-1}. The precursors were mixed prior to the nozzle and then atomized by a gas-assisted external mixing nozzle by oxygen (flow rate of dispersion gas was 583 cm^3 s^{-1}). This combustible aerosol was ignited by six acetylene–oxygen flamelets (flow rates, C_2H_2=217 cm^3 s^{-1}, O_2=283 cm^3 s^{-1}). The produced particles were collected in a bag house filter system, and representative samples (1–2 g) were collected on glass fibre filters (GF/A 150, Whatman) via a bypass using vacuum pumps.

Characterization of Nb-doped TiO_2

The specific surface area (SSA) of as-prepared powders was determined from a five-point N_2 adsorption isotherm obtained from Brunauer–Emmett–Teller (BET) measurements using a Beckman Coulter SA3100. Prior to analysis, powder samples were dried at 180°C for 120 min in nitrogen atmosphere to remove physisorbed water from the surface.

X-ray diffraction (XRD) analysis was performed with a Philips PANalytical X'Pert Pro MPD diffractometer using Cu Kα filtered radiation over a 2θ range from 10° to 80°. The XRD results were used to determine the phase composition and the resulting anatase/rutile volume ratio. Phase identification was carried out using the Inorganic Crystal Structure Database (ICSD).

Particle size, shape and morphology of flame-made TiO_2:Nb nanopowders were investigated by scanning and transmission electron microscopy (STEM-TEM). TEM images were recorded with a high-resolution and analytical STEM-TEM JEOL 2200FS equipped with an omega filter for energy-filtered imaging. The powder samples for TEM measurements were deposited onto carbon-coated copper grids (Plano GmbH).

The band gap energy (E_g, energy of the fundamental optical transitions from the valence band to the conduction band) was derived from optical diffuse reflectance spectra R (λ). Spectrophotometric measurements were performed with a Lambda 19 Perkin-Elmer double-beam spectrophotometer, equipped with a 150 mm integrating sphere and used to measure the spectral dependence of total and diffuse reflectance in the wavelength range from 250 to 2,500 nm.

Photocatalytic experiments

Three different aqueous (deionized water with pH=5.5) solutions 5.13×10^{-5} M methylene blue (MB), 5.19×10^{-5} M methyl orange (MO) and 1.00×10^{-3} M 4-chlorophenol (4-CP) were prepared for photoactivity evaluation experiments. The pH of MB solution was 5.5, and the pH of MO solution was 4.5, and no adjustment of pH was done. The pH of 4-CP solution was adjusted with 1 M perchloric acid to final value of pH=2, following Mills et al. (1993). The powder concentration was kept constant at 0.4 mg/cm^3. The reaction suspension of the powder in the pollutant solution was subjected to an ultrasound treatment for 10 min. The photocatalytic experiments were carried out in a photochemical photoreactor Lidam. The details of the setup are given elsewhere (Mills et al. 1993; Mills and Morris 1993). In brief, the photochemical irradiation system comprised two half cylinders, each of them contained six Sylvania Blacklight Blue F8W/BLB T5 ($\lambda_{max.}$=355−360 nm) for UVA irradiation, LCD Lightening Inc. M2-65-01 Hg lamps ($\lambda_{max.}$=435 nm) for the visible light irradiation. The reaction vessel was a double-walled 125 cm^3 quartz Drechsel bottle fitted with a rubber septum through which the samples were extracted. Thermostated water (30 °C) was pumped continuously through the outer jacket of the reaction vessel during the experiments. A sample of the photocatalyst was dispersed in a reaction solution and was filled into the inner part of the reaction vessel, magnetically stirred (300 rpm) and continuously purged with air (110 ml/min) from the central line over the irradiation period. Extracted samples were filtered through membrane filters (0.2 μm Nylon, Roth Rotilabo®) into PMMA cuvettes (Roth). Samples were extracted at fixed time intervals and characterized by a UV–VIS Varian Cary 50 SCAN spectrophotometer. Calibration of the absorbance at 664 nm against MB concentration, at 464 nm against MO concentration and 280 nm against 4-CP concentration (Lambert–Beer Law) was carried out for the determination of the photocatalytic activity (PCA), and the concentration was determined from the peak intensity.

Results and discussion

Structural properties of TiO_2:Nb nanopowders

The specific surface area of as-synthesized powders varied as a function of the doping amount from 42.9 m^2/g for TiO_2:0.1 at.% Nb to 90 m^2/g for TiO_2:15 at.% Nb doped (Table 1). The increase of SSA with higher Nb level is determined by the synthesis parameters. As it can be seen in Fig. 1, there is a correlation between the precursor mole number (n_{prec}) and SSA. Namely, a higher precursor mole number per time unit results in lower SSA because a higher supersaturation in the flame is reached from which bigger particles result. The total feed flow rate (FR_{Total}) was kept constant during synthesis routine. In order to increase Nb concentration in TiO_2 nanoparticles, feed flow rate of Nb precursor was increased and feed flow rate of main precursor titanium tetraisopropoxide TTIP (FR_{TTIP}) decreased. This resulted in a simultaneous increase of the Nb level in TiO_2 and SSA of the powder.

The morphology of TiO_2:Nb nanopowders was observed by TEM. The TEM images (Fig. 2) showed that flame-made TiO_2:Nb nanopowders consist of nanosized, spherically shaped and crystalline particles. The size distribution of the TiO_2-based particles was the broadest for powders containing 0.1 at.% Nb as it was covering a particle size from 10 up to 90 nm, with an average size of 40 nm (Fig. 2a). The size of TiO_2 particles with 5 at.% Nb varied between 5 and 90 nm; however, it can be clearly seen from Fig. 2c that the average particle size is smaller (28 nm) than for particles with a lower Nb content (Fig. 2a). For a 15 at.% Nb level, the particle size remained below 30 nm (average size, 14 nm), and no large particles were observed (Fig. 2e).

Table 1 Structural parameters of TiO_2:Nb and TiO_2-P25 nanopowders

Sample name	SSA/m^2 g^{-1}	d_{BET}/nm	wt% rutile	$d_{XRD,\ A}$/nm	d_{TEM}/nm
TiO_2-P25[a]	49.1	30.9	16.9	21	–
TiO_2:0.1 at.% Nb	42.9	35.8[b]	–	–	39.9
TiO_2:0.5 at.% Nb	47.7	35.8	2.8	31.0	–
TiO_2:1 at.% Nb	52.0	32.2	3.3	33.6	–
TiO_2:5 at.% Nb	66.7	29.3	3.5	22.3	27.6
TiO_2:10 at.% Nb	82.0	22.7	2.5	13.4	–
TiO_2:15 at.% Nb	90.0	18.4[b]	–	–	14.5

[a] $d_{XRD,\ R}$=35 nm

[b] d_{BET} calculated with assumption of 3 wt% of rutile

The selected area electron diffraction (SAED) pattern taken for the TiO_2 particles with 0.1 at.% of Nb consists mainly of spots, which are generated by the largest particles (inset of Fig. 2b). No preferential orientation of the particles could be observed. Conversely, the SAED pattern of the particles containing 15 at.% Nb is composed of rings with rare distinct spots, confirming the reduction of the particle size and their random distribution.

The diffraction patterns consisting of sharp rings with spots and the high-resolution images confirmed the crystalline character of the powders. The high-resolution TEM images (HRTEM), Fig. 2b, d, and f, clearly show differently oriented lattice fringes for the different particles. Independently on their size, the particles were not single crystalline, but contained grain boundaries and hence multiple grains with different lattice orientations within a single particle. The surface layer of the particles seemed to have an amorphous character and some of the smallest particles, with sizes below 10 nm seemed to be amorphous (Fig. 2f). The energy-filtered mapping (EFTEM), inset in Fig. 2c, e, confirmed the presence and of Ti, O and Nb in the analysed particles. The distribution of these three elements in the particles was uniform up to 5 at.% Nb. In the case of particles with 15 at.% Nb, also high concentrations of Nb on the surface were detected (inset in Fig. 2e, dominating purple colour, which indicates presence of Nb). This effect was also confirmed by XRD results (Fig. 3). Samples with higher level of Nb doping are not homogenous, and traces of additional phase can be detected. Presence of such Nb-rich zones in the photocatalytic material can negatively affect photoactivity through an enhancement of the recombination process.

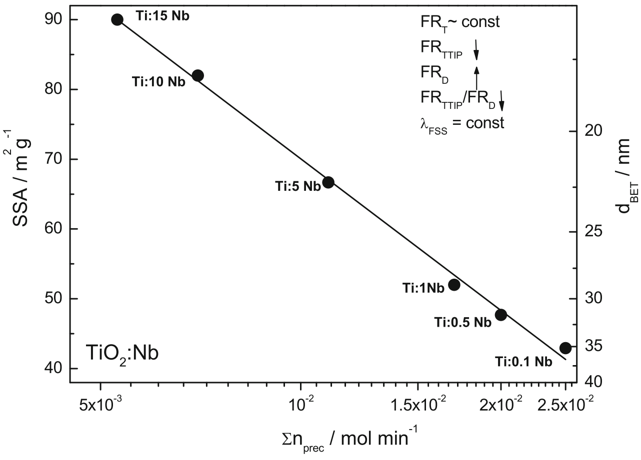

Fig. 1 The specific surface area (SSA) and the particle size (d_{BET}) of TiO_2:Nb nanopowders as a function of total precursor concentration

Effect of niobium on TiO_2 crystallinity and phase composition was investigated by XRD measurements (Fig. 3). The intensities of the anatase reflection at 2θ=25.4° and the rutile reflection at 2θ=27.5° were analysed, and the percentage of rutile in the samples was determined using the following equation, Eq. 1 (Spurr and Myers 1957).

$$\chi = \left(1 + 0.8\frac{I_A}{I_R}\right)^{-1} \quad (1)$$

Where, χ is the weight fraction of rutile in the powder, I_A and I_R are peak intensities of anatase and rutile phase, respectively.

FSS-made nanopowders are well crystalline as was expected from elaboration procedure since the flame spray synthesis is a one-step process, which allows obtaining crystalline powders owing to high temperature in the flame (Akurati et al. 2008). XRD patterns of the here presented FSS-made powders show that as-prepared nanopowders consist mainly of anatase phase (96–98 wt%), which is the desired phase for the photocatalytic application. Besides anatase, rutile reflections can be observed as a second phase. Additional niobium oxide phase was formed at about 5 at.% of Nb doping, which can be seen as reflections at 2θ=28.6°, 2θ=33.0° and 2θ=14.5°. These reflections are probably attributed to monoclinic Nb_2O_5, the most common and stable niobium oxide. A left shift of XRD pattern follows increasing level of niobium, which indicates an enlargement of unit cell (inset in Fig. 3). It originates from the value of ion radius of Nb^{5+} (0.69 Å), which is slightly bigger than ion radius of Ti^{4+} (0.64 Å) (Shannon 1976). Additionally, peak broadening was observed for powders with higher Nb level due to the smaller particle size.

Fig. 2 TEM (**a**, **c**, **e**) and HRTEM (**b**, **d**, **f**) images of TiO_2:Nb nanopowders: **a**–**b** TiO_2:0.1 at.% Nb, **c**–**d** TiO_2:5 at.% Nb, **e**–**f** TiO_2:15 at.% Nb. *Insets* in **b** and **f** SAED patterns and *insets* in **c** and **e** EFTEM map of Ti (*blue*), O (*yellow*) and Nb (*purple*)

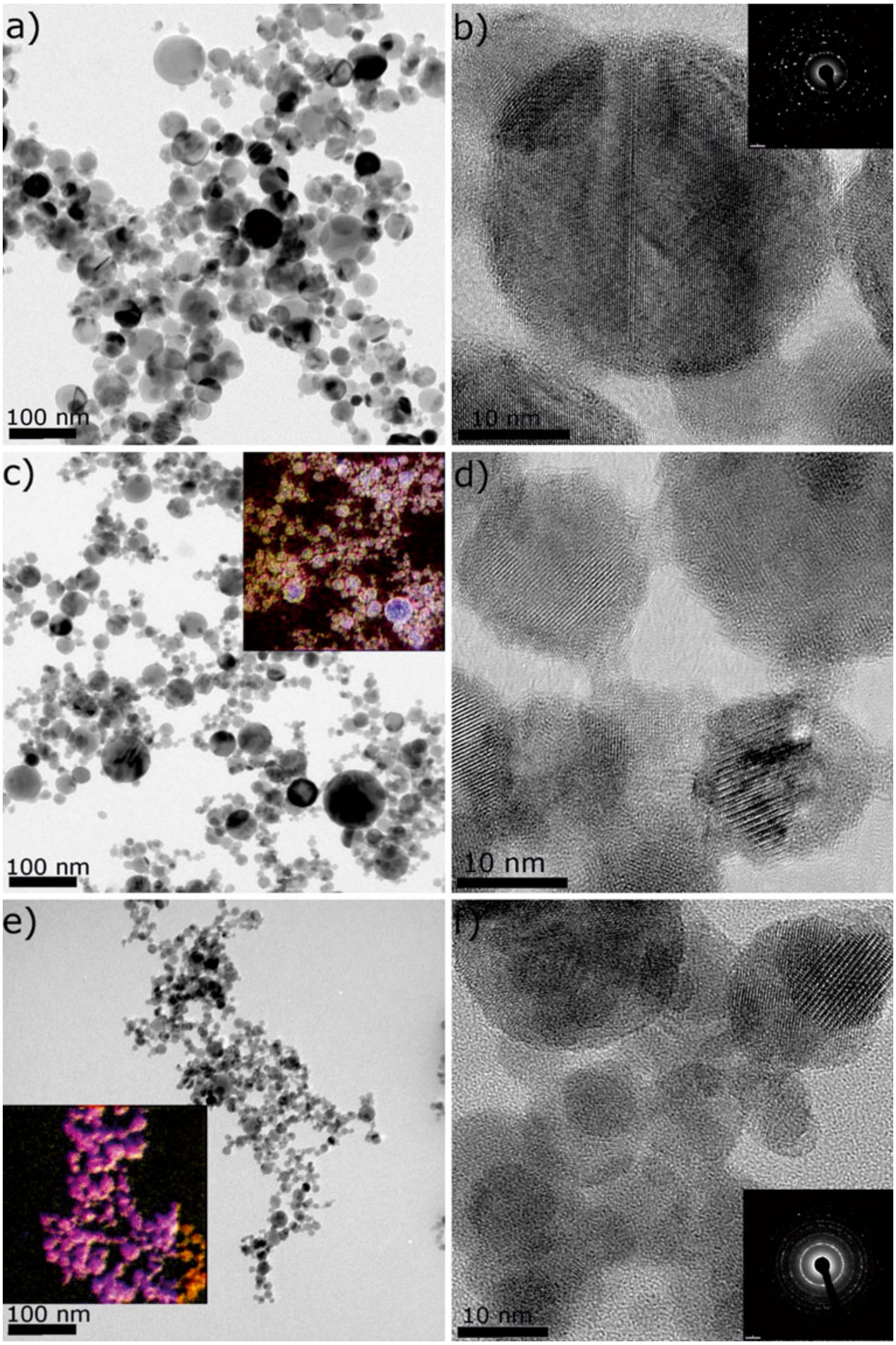

Anukunprasert et al. (2005) established that phase modification for TiO_2:Nb nanopowders can be observed when TiO_2 is doped with more than 3 mol% Nb. Three to five mole percent of Nb hinders the anatase to rutile transformations, and only anatase polymorph was observed. Trenczek-Zajac et al. (2006, 2007) observed that samples containing more than 10 at.% of Nb are not homogenous, and traces of an additional titanium niobate phase were detected for samples with 15 at.% Nb. Zaitsev et al. (2000) reported that the solubility limit of Nb was more than 5 mol% in anatase, whereas Traversa et al. (2001) report up to 5 at.% and Ruiz et al. (2003) of about 10 at.% of Nb in anatase. Sheppard et al. (2006) found no evidence of another phase than anatase up to 40 at.% of Nb. Tsvetkov et al. (2011b) showed that increase of Nb concentration resulted in decrease of rutile phase and for TiO_2:3 mol% Nb only anatase phase was detected. Kubacka et al. (2009)

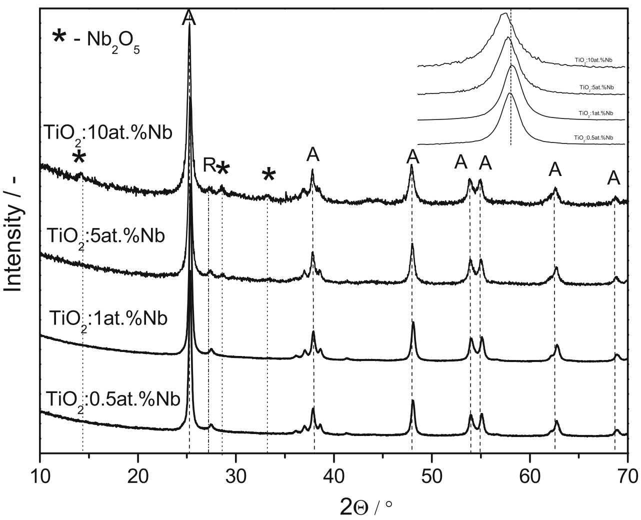

Fig. 3 XRD pattern of TiO_2:Nb with increasing level of doping; *inset* shows enlargement at 2θ=25.4°

obtained TiO_2 doped with 9.7 and 20.2 at.% Nb and observed that Nb displays a solubility limit, which can be seen as Nb-rich local zones and arrangements within the anatase. Such a discrepancy among results reported in the literature can be related to a variety of used synthesis methods. Therefore, it can be assumed that niobium substitutes titanium in the crystal lattice up to a certain level of Nb doping, which seems to be strongly dependent on the material preparation technique. It seems difficult to establish the solubility limit of Nb in anatase since anatase-to-rutile transformation phase occurs at 973−1,173 K and the conditions of the thermodynamic equilibrium are not defined (Sheppard et al. 2006). Uncertainty in the identification of the additional phase next to anatase and rutile can be connected with the presence of some variations in the determination of exact position of the peak, arising from the hindered alignment during profile fitting. Nevertheless, there are few reports on TiO_2:Nb claiming a presence of traces of niobium species, such as NbO_2 or Nb_2O_5 (Zaitsev et al. 2000; Ruiz et al. 2003), with indication on the report of Teleki at al. (2008) on presence of Nb_2O_5 in FSS-made TiO_2:10 at.% Nb nanopowder.

From the results obtained by XRD and BET measurements, particle size was calculated according to the following equation (Eq. 2):

$$d_{\mathrm{BET}} = \frac{6,000}{(V_{\mathrm{A}} \times \rho_{\mathrm{A}} + V_{\mathrm{R}} \times \rho_{\mathrm{R}} + V_{\mathrm{Nb}} \times \rho_{\mathrm{Nb}}) \times \mathrm{SSA}} \qquad (2)$$

where, V_A, V_R, V_{Nb} and ρ_A, ρ_R, ρ_{Nb} are the volume fractions determined from the XRD patterns and the densities of anatase-TiO_2, rutile-TiO_2 and Nb_2O_5, respectively (ρ_A=3.84 g/cm^3, ρ_R=4.25 g/cm^3 and ρ_{Nb}=4.47 g/cm^3). Values of density were taken after ICSD data files. The average mean crystallite size of anatase was calculated from Scherrer's equation (Eq. 3) (Ogawa et al. 1981) using the full-width-at-half-maximum value of the anatase diffraction peak:

$$L = \frac{K \times \lambda}{(\beta \times \cos\theta)} = d_{\mathrm{XRD}} \qquad (3)$$

where, L is the crystallite size, λ is the wavelength of the X-ray radiation (Cu Kα 1.540598 Å), K is 0.89 and β is the line broadening at the half-maximum intensity after subtraction of equipment broadening. The average crystallite size was in the range of 13.4 to 35.0 nm. According to Almquist and Biswas (2002), such grain sizes are the most suitable for photocatalytic applications. The obtained $d_{\mathrm{XRD,\,A}}$ are in relatively good agreement with BET (d_{BET}) and TEM (d_{TEM}) measurements. TEM measured average particle size (d_{TEM}) and geometric standard deviation (σ_g) of TiO_2 with 0.1, 5 and 15 at.% Nb were calculated based on TEM images, Fig. 2a, c and e. d_{TEM} and σ_g were derived from log-probability plots. Particle size distribution curves are presented in Fig. 4, and calculated σ_g values between 1.5 and 1.7 are slightly larger than common flame-derived particle size distribution (PSD). It is probably due to usage of $NbCl_5$, an inorganic salt which is nonvolatile and leads to a broadening of the PSD (Messing et al. 1993). To explain the small discrepancy between d_{XRD}, d_{BET} and d_{TEM} values, it should be noticed that a secondary rutile phase is present in the samples, which was not taken into account for d_{XRD} evaluation. Moreover, one should consider that all methods of particle size determination are based on different assumptions, and in the case of X-ray diffraction, the average crystallite size is obtained and not the particle size, as for BET or TEM.

Optical properties of TiO_2:Nb nanopowders

Evaluation of optical properties of the photocatalyst is of a great importance. The band gap energy of such a material determines the range of irradiation under which the photocatalyst can be

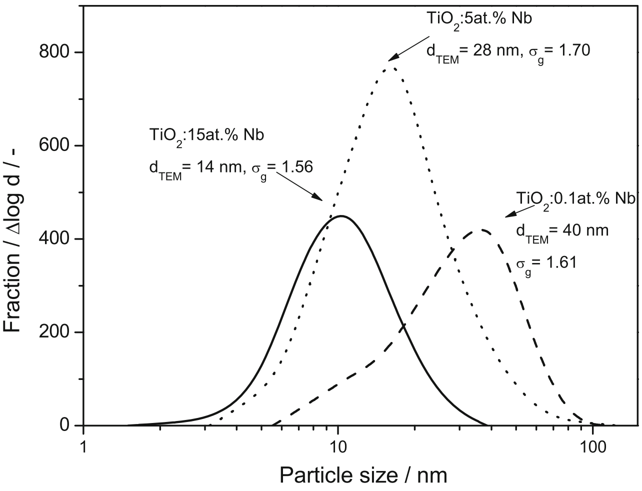

Fig. 4 Particle size distribution of TiO_2 with 0.1, 5 and 15 at.% Nb nanopowders calculated from TEM images

efficiently applied. Therefore, it is crucial to investigate optical properties and resulting optical transitions in flame-made TiO_2:Nb nanopowders especially because contradicting reports regarding the effect of Nb on the optical properties of TiO_2 can be found in literature. Wang et al. (1995) reported a band gap shift from 3.03 eV for TiO_2 to 2.9 eV for TiO_2:0.5 mol% Nb, where the given TiO_2 band gap is a literature value and the one for TiO_2:0.5 mol% Nb is an experimental one. Similarly, Mattsson et al. (2006) reported about the red shift of the fundamental absorption edge from 394 nm (3.15 eV) for undoped TiO_2 to 411 nm (3.02 eV) for 20 at.% of Nb doping. In contrast to this, Gautron et al. (1983) reported no band shift for TiO_2-NbO_2 solid-state solution with 20 at.% Nb.

Diffuse reflectance spectroscopy was used to evaluate the optical properties and the band gap of flame-made TiO_2:Nb nanopowders. The increase of Nb concentration decreases the diffuse reflectance (R_{diff}) in the visible range, which indicates improved light absorption in this range (Fig. 5). In TiO_2 with low doping level from 0.1 to 1 at.% Nb, a strong reduction of R_{diff} intensity is observed in the range of 500–800 nm and a moderate one in the fundamental absorption region (Fig. 5a). For TiO_2: 5 at.% Nb nanopowder, the slope of the R_{diff} intensity shift is not steep, and for 10 at.% Nb, it reaches a plateau which is again shifted to lower intensity for 15 at.% Nb (Fig. 5b). The difference of R_{diff} for TiO_2 with lower (0.1–1 at.%) and higher (5–15 at.%) niobium content can be related to the presence of secondary phase. In flame-made TiO_2 nanopowders, the solubility limit was exceeded for Nb level >1 at.%. This means that up to 1 at.% Nb, no Nb-related secondary phase was detected, and it can be assumed that Nb^{5+} substitutes Ti^{4+}. In case of 5 at.% or higher Nb concentration, the material is heterogeneous, and the additional electron transitions can occur due to this fact. Nb_2O_5 is present most probably on the TiO_2 surface and therefore lowers R_{diff} intensity. The particle size is an another factor which can have an influence on the different trend of TiO_2:Nb with low and with high dopant level. As already mentioned (Table 1), nanopowders with the 0.1–1 at.% Nb doping level have a comparable particle size (~35 nm), and therefore, the main effect of the enhanced light absorption in the visible range can be assigned to the increased Nb level. In case of TiO_2 with higher doping levels, the increased level of niobium doping is followed by the reduction of the particle size (d_{BET}) from 24 nm for TiO_2:5 at.% Nb to 18 nm for TiO_2:15 at.% Nb. This results in more surface-related defects and can also cause the change in the R_{diff} spectra.

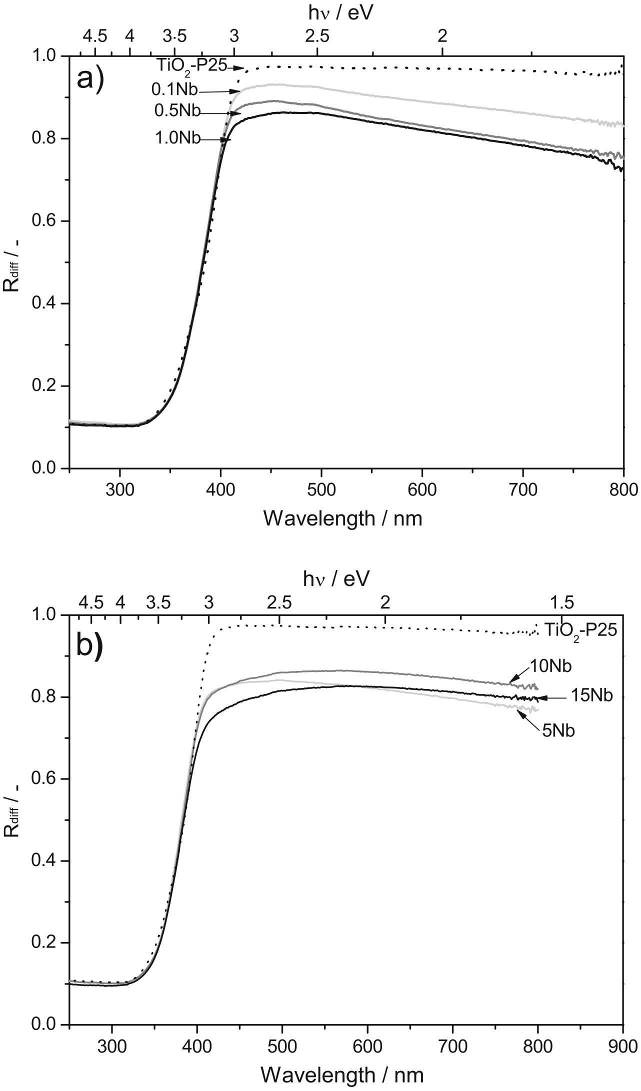

Fig. 5 Diffuse reflectance spectra **a** of TiO_2 doped with 0.1, 0.5 and 1 at.% Nb and **b** of TiO_2 doped with 5, 10 and 15 at.% Nb nanopowders compared with TiO_2-P25 nanopowder

The band gap energy (E_g) and the doping-related electronic transitions were evaluated from the peak maximum of the differential reflectance spectra (dR_{diff}) vs. wavelength (Fig. 6). This is the most appropriate method of the band gap estimation for well-crystalline semiconductor materials (Radecka et al. 2006; Michalow et al. 2009b). For the commercial TiO_2-P25 (Fig. 6a), differential reflectance spectrum was fitted with two Gaussian plots $E_{g2}=3.31$ eV and $E_{g3}=3.11$ eV, which can be assigned to the electronic transition in the anatase and rutile phase, respectively (Table 2). Beside the peaks related to the anatase (E_{g2}) and rutile (E_{g3}) phase, a third E_{g1} can be distinguished at shorter wavelengths from the TiO_2-FSS dR_{diff} spectra (Fig. 6b). The electronic transition at E_{g1} is derived from the amorphous phase, which is slightly shifted to a higher energy and can be present in as-prepared samples due their high surface area (Tian et al. 2005; Ohtani et al. 1997). As can be seen on Fig. 6c, d, niobium doping in TiO_2 caused an appearance of an additional electronic transition E_{g4} around 2.8 eV (Table 2), beside already assigned E_{g1}, E_{g2} and E_{g3}. Mulmi et al. (2004) revealed also an additional absorption band at 2.2 eV in Nb-doped anatase single crystal. This additional absorption was explained by a

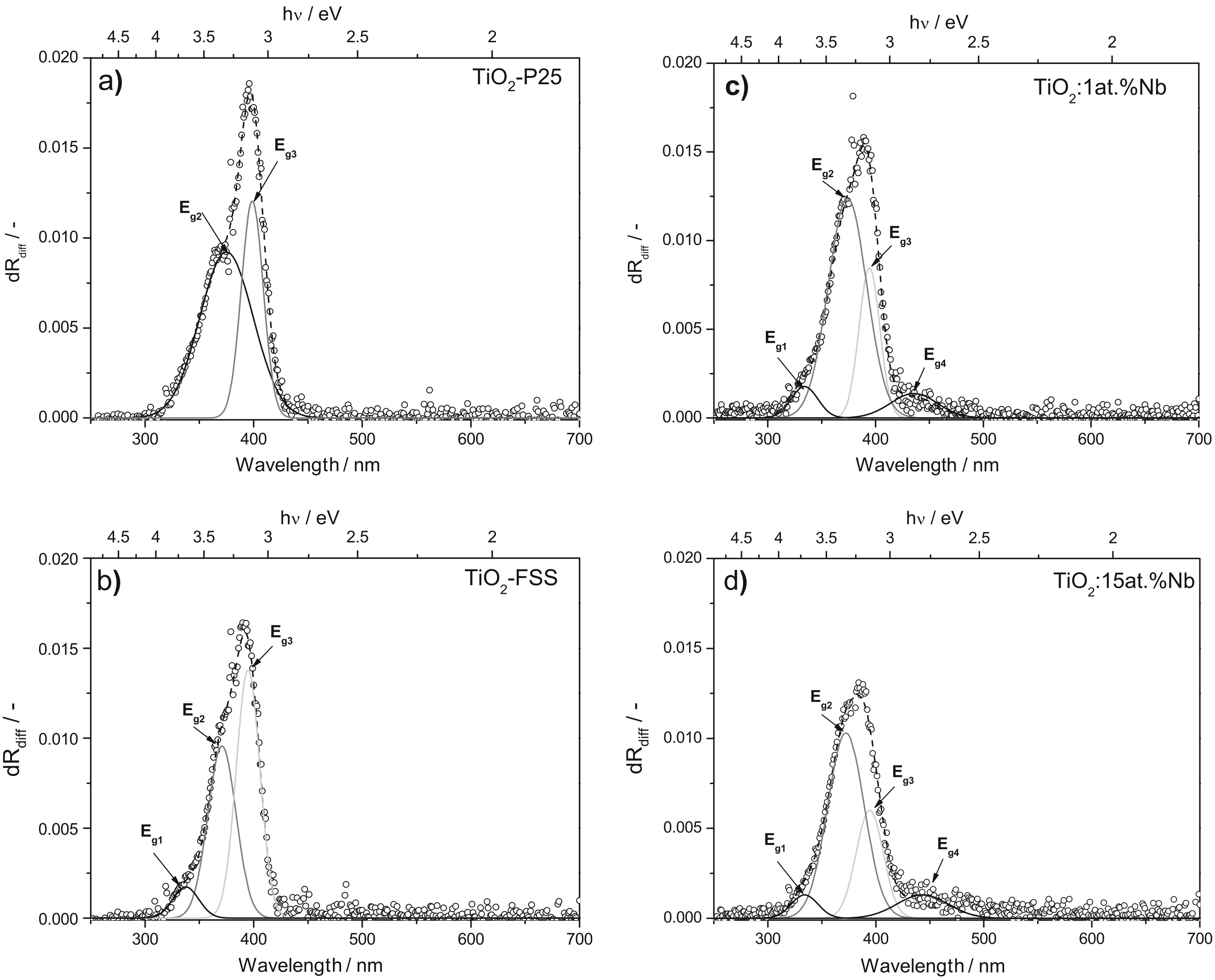

Fig. 6 The differential reflectance spectra of **a** TiO_2/P25, **b** TiO_2-FSS, **c** TiO_2:1 at.% Nb and **d** TiO_2:15 at.% Nb nanopowders vs. wavelength and energy fitted by Gaussian plots, where E_{g1}, E_{g2}, E_{g3} and E_{g4} indicate transition energy for amorphous TiO_2, anatase phase, rutile phase and doping, respectively

d-d transition in the conduction band. With increased level of niobium, a slight shift of the dopant-related transitions towards longer wavelengths was observed. Since Nb^{5+} is a donor type of dopant, it can be assumed that the dopant-related level is located under the conduction band within the band gap. Each applied doping level of niobium affected the electronic structure of TiO_2. According to literature (Stone and Davis 1998), it was not possible to distinguish the Nb_2O_5-related electronic transition, which is located at around 3.3 eV in TiO_2:Nb nanopowders with Nb>1 at.%. There are also no reports about such observation even for samples up to 20 at.% Nb of doping (Mattsson et al. 2006). As can be seen from Fig. 6c, d, the overall intensity of the differential spectra lowers with increased Nb concentration. It is probably related to the increased number of defects with higher Nb content as well as increased number of surface-related defects since the particles size changes from 35 nm for TiO_2:1 at.% Nb to 18 nm for TiO_2:15 at.% Nb. On the other hand, the relative intensity of transition at ~2.8 eV is slightly higher for higher doping. However, it should not be taken as an absolute value since there are several other factors which can have an influence on the dR_{diff} intensity.

Table 2 Transition energy levels of TiO_2:Nb and TiO_2-P25 nanopowders

Sample name	E_{g1}/eV	E_{g2}/eV	E_{g3}/eV	E_{g4}/eV
TiO_2-P25	–	3.31	3.11	–
TiO_2:0.1 at.% Nb	3.75	3.31	3.12	2.87
TiO_2:0.5 at.% Nb	3.71	3.32	3.13	2.87
TiO_2:1 at.% Nb	3.71	3.32	3.14	2.85
TiO_2:5 at.% Nb	3.71	3.32	3.14	2.83
TiO_2:10 at.% Nb	3.71	3.32	3.14	2.81
TiO_2:15 at.% Nb	3.71	3.33	3.14	2.80

Photocatalytic activity

The photocatalytic activity of flame-made TiO_2:Nb nanopowders was evaluated under UVA and VIS irradiation. As model pollutants, methylene blue (MB), methyl orange (MO) and 4-chlorophenol (4-CP) were chosen.

Methylene blue (Lakshmi et al. 1995; Mills and Wang 1999; Houas et al. 2001; Awati et al. 2003) and methyl orange (Almquist and Biswas 2002; Sclafani and Herrmann 1996) are representatives of cationic and anionic type of pollutant. 4-Chlorophenol is an inert molecule with a benzene ring structure, which allows capture of the radical intermediates or the direct interaction with an electron (Mills et al. 1993; Mills and Morris 1993; Hoffmann et al. 1995; Linsebigler et al. 1995; Mills and Davies 1995; Guillard et al. 1999; Herrmann et al. 1999). Langmuir–Hinshelwood kinetic model was used to evaluate kinetics of the photocatalytic performance of TiO_2:Nb nanopowders as a function of niobium concentration (Figs. 7 and 9) (Yang et al. 2005). The apparent first-order photodecomposition kinetic rate constant (k_{app}) was calculated on the basis of $\ln(C/C_0)$ vs. time plots, which show a linear dependence. The slope of $\ln(C/C_0)$ vs. time allows to calculate the k_{app} value. For k_{app} calculation of photocatalytic performance under UVA irradiation, the first 15 min of the reaction was taken into account, while in the case of VIS irradiation, 180 min of the reaction was considered. Adsorption of the pollutant on the photocatalysts surface is an important step in photodecomposition processes (Fox and Dulay 1993). That is why the time (10 min) needed for adsorption of the pollutant on the surface of the photocatalysts was included in the evaluation of the photocatalytic kinetic rate. All the obtained photocatalytic results were compared to commercially available TiO_2-P25 (Evonik Industries AG) nanopowder. TiO_2-P25 became a research standard due to its reasonably well-defined nature (Table 1) and its high photoactivity in the UV range.

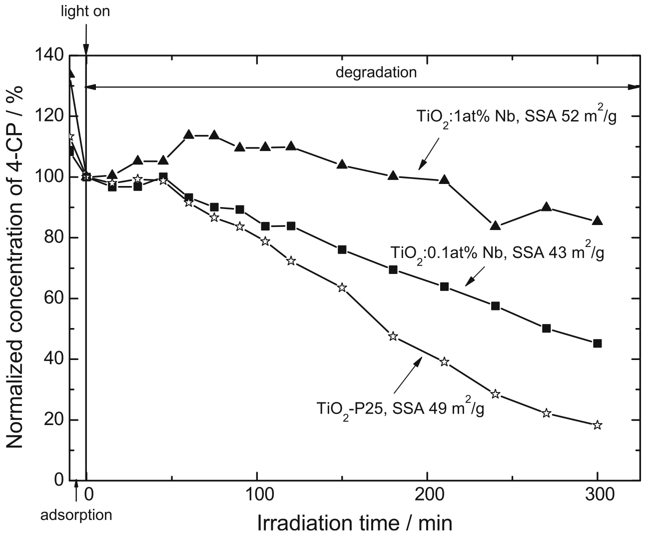

Fig. 8 Degradation of 4-CP with TiO_2:Nb and TiO_2-P25 under UVA irradiation. Negative time (−10 min) indicates the period of 4-CP adsorption on the surface of photocatalyst

Figure 7 shows a photodecomposition of MB and MO in the presence of TiO_2:Nb nanopowders under UVA irradiation. PCA of TiO_2:Nb nanopowders for MB degradation was investigated over the whole range of niobium concentration. There is no clear trend of PCA with the niobium concentration. TiO_2:5 at.% Nb nanopowder showed the lowest photocatalytic performance since it consists not only of anatase and rutile but also of a Nb_2O_5 phase. PCA rises when the niobium level is higher than 5 at.%. This improved performance can be explained as follows: with higher Nb concentration, the specific surface area (SSA) increases and a particle size decreases (Fig. 1 and Table 1); therefore, photoinduced charges have a shorter path towards the

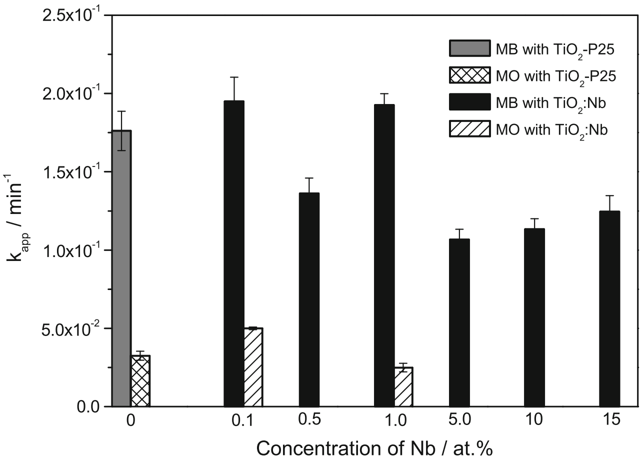

Fig. 7 Comparison of apparent first-order photodecomposition kinetic rate constant (k_{app}) of MB and MO under UVA irradiation in the presence of TiO_2:Nb and TiO_2-P25 as a reference

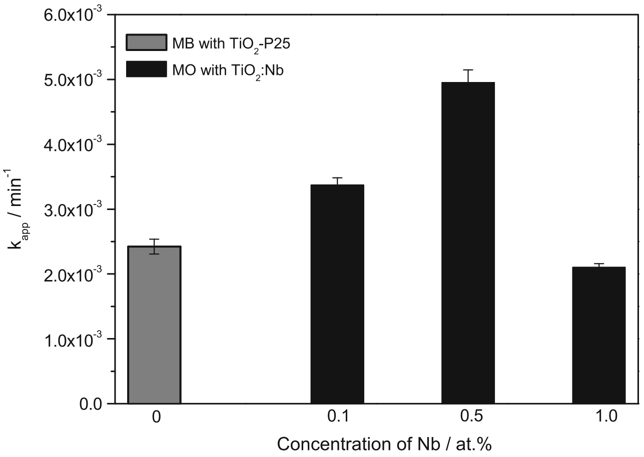

Fig. 9 Comparison of apparent first-order photodecomposition kinetic rate constant (k_{app}) of MB under VIS irradiation in the presence of TiO_2:Nb and TiO_2-P25 as a reference

particle surface. High SSA means a high reactive surface towards both light absorption and pollutant adsorption. Another important factor is an increased dopant concentration and its effect on the defect creation, which can act both as active and recombination centres. Nb^{5+} acts as a donor type of dopant while substituting Ti^{4+} in the cationic sublattice. This requires a charge compensation to assure electroneutrality of the whole crystal. The most probable charge compensation mechanism for TiO_2 doped with Nb<10 at.% is the formation of titanium vacancies (Sheppard et al. 2006), which is in accordance to the following Nb_2O_5 incorporation into TiO_2 crystal lattice (Radecka and Rekas 1995):

$$2Nb_2O_5 \leftrightarrow 4Nb_{Ti}^{\cdot} + V_{Ti}'''' + 10O_o \tag{4}$$

It was also reported (Nowotny et al. 2006) that titanium vacancies located at or near the surface are responsible for water adsorption and therefore for an improvement of photocatalytic performance. Hence, it can be concluded that titanium vacancies introduced by Nb^{5+} doping can act as active centres of hydroxyl radical formation. On the other hand, Finklea (1988) reported that Nb doping increases the charge carrier density. Charge compensation for donor doping in this case was achieved by electron localization on Nb^{4+} at 0.12 eV below the conduction band, which can act as shallow traps and therefore as recombination centres. So, the electroneutrality condition assumes the form:

$$\left[Nb_{Ti}^{\cdot}\right] = 4\left[V_{Ti}''''\right] + [e'] \tag{5}$$

Increased niobium content enhanced the surface acidity as was observed on the basis of improved adsorption of MB in darkness. From total MB concentration, 6.5 and 16.5 % were adsorbed by TiO_2:0.1 at.% Nb and TiO_2:15 at.% Nb, respectively, during equilibration time before the irradiation was switched on. In comparison, TiO_2-P25 adsorbed 1.8 % of the total MB amount under the same conditions. TiO_2:0.1 at.% Nb and TiO_2:1 at.% Nb nanopowders showed the best performance towards MB photodecomposition, even 1.11 times higher than TiO_2-P25. Therefore, these two powders were chosen for further experiments towards photocatalytic decomposition of MO under UVA irradiation. As can be seen from Fig. 7, TiO_2:0.1 at.% Nb shows also good PCA for another type of pollutant, and k_{app} is 1.54 times higher than the one of TiO_2-P25. However, pure TiO_2-P25 shows better adsorbance of MO than any TiO_2:Nb nanopowder. TiO_2-P25 adsorbed 21.8 % of total MO concentration, whereas TiO_2:0.1 at.% Nb and TiO_2:1 at.% Nb adsorbed 17.5 and 14.6 %, respectively. Based on these results, it can be concluded that both pollutants have different interaction with the surface of TiO_2:Nb nanoparticles, which is related to the fact that MB is a cationic type of dye and MO is an anionic type of molecule. The apparent first-order kinetic rate constant for MO degradation is four times lower than the one for MB degradation in the presence of TiO_2:0.1 at.% Nb under UVA irradiation. Therefore, for further experiments under UVA irradiation, 4-chlorophenol was chosen as a model inert molecule. TiO_2:0.1 at.% Nb and TiO_2:1 at.% Nb were selected due to their good activity under UVA irradiation. However, their performance is worse than of TiO_2-P25. In case of TiO_2-P25 and 5 h of irradiation, 18.3 % of the total 4-CP amount remained, while in case of TiO_2:0.1 at.% Nb, it was 45.2 %. On the left hand side of Fig. 8, it can be seen that with an increased concentration of Nb, the adsorption of 4-CP increased. For TiO_2:1 at.% Nb 25.3 % of total 4-CP concentration was left. Here, it has to be admitted that evaluation of 4-CP concentration by spectroscopic measurements was difficult due to the intermediate products which have an absorption in the range of 4-CP (Mills et al. 1993; Mills and Morris 1993).

In the next step, the photocatalytic performance of TiO_2:Nb nanopowders with low Nb concentration towards MB and MO decomposition was tested under VIS irradiation (λ_{max}=435 nm). TiO_2:0.1 at.% Nb and TiO_2:0.5 at.% Nb showed higher performance than TiO_2-P25 for MB decomposition. TiO_2:0.5 at.% Nb performed even two times better than the commercial photocatalyst (Fig. 9). It is very interesting that the photocatalytic activity under VIS irradiation showed a reverse trend to the one under UVA irradiation if TiO_2 nanopowders with low concentrations of Nb are used. None of the investigated materials showed a photocatalytic activity towards MO or 4-CP. Lack of photocatalytic activity towards MO decomposition under VIS irradiation can be explained by a lack of light available for photocatalyst excitation caused by full overlap of absorption spectra of MO with emission spectra of applied VIS irradiation. One should expect a high rate of dye photodecomposition through the photosensitized catalysis. However, this effect did not occur in the studied system. It can be explained by a non-proper location of the redox potential of $MO^{*}/MO^{\bullet+}$ with respect to the conduction band of photocatalyst. Therefore, transfer of the electron from an excited dye molecule to photocatalyst is not possible. In the case of 4-CP, a lack of activity of TiO_2:Nb under VIS irradiation and low activity under UVA irradiation can be explained by a type of charge transfer in the investigated material.

To summarize, TiO_2:Nb flame-made nanopowders with niobium concentration in the range from 0.1 to 1 at.% showed better photocatalytic performance towards MB decomposition under UVA and VIS irradiation than TiO_2-P25. Observed enhancement can be related not only to the preferable anatase structure of TiO_2:Nb nanoparticles in comparison to TiO_2-P25 but also to a good crystallinity and optimal spherical shape and size (~35 nm) of the particles as well as to an improved surface acidity and therefore higher affinity towards water and hydroxyl groups adsorption due to the niobium doping (Onfroy et al. 2007; Akurati et al. 2008; Cui et al. 1995). The study of photocatalytic degradation of different types of pollutants like MB, MO and 4-CP representing cationic, anionic and inert type of molecules, respectively, by TiO_2:Nb nanopowders showed that photocatalysis is a selective type of reaction, and not all types of pollutants interact in the same way with the photocatalyst surface. Further on, they do not follow the same degradation path and therefore show different degradation kinetics. These facts can be taken as an advantage when a selective type of photocatalyst is required.

Under VIS irradiation, TiO_2:0.1 at.% Nb and TiO_2:0.5 at.% Nb showed a better performance towards MB decomposition than TiO_2-P25. In all cases, decomposition of MB and MO was followed by a lowering of pH, which indicates complete decomposition of MB and MO molecules and not only a decolorization process (Michalow et al. 2008). The good performance of TiO_2:Nb nanopowder can be related to an improved electronic conductivity and an additional transition energy level located at 2.8 eV, which is directly irradiated by applied VIS irradiation. However, a question occurs as to why TiO_2-P25 showed any photocatalytic performance towards MB degradation under VIS irradiation. It is probably due to the photosensitized type of the reaction, where MB dye molecule is photoexcited instead of the photocatalyst. An electron is transported from the photoexcited MB to the conduction band of a photocatalyst and reacts then, e.g. with O_2 molecule, which is an electron scavenger, and a superoxide radical is created. These radicals can further react towards complete decomposition of MB. It seems that even a very small overlap of the adsorption spectra of MB and the applied irradiation is sufficient to drive the photosensitized type of reaction (Yan et al. 2006; Mills and Wang 1999). This can as well explain the lack of photocatalytic activity of investigated materials towards 4-CP decomposition under VIS irradiation. In case of colourless 4-CP molecule with an adsorption maximum at 280 nm the photosensitization reaction cannot occur.

Conclusion

TiO_2:Nb nanoparticles were successfully obtained by liquid-fed one-step flame spray synthesis. Obtained particles were spherically shaped and well crystalline. Up to 1 at.% Nb nanopowder was composed mainly of anatase (~96 wt%) and a small amount of rutile. Up from 5 at.% of niobium formation of a Nb_2O_5 phase was observed, which was homogenously dispersed on the TiO_2 surface. Niobium doping caused a decrease of a diffuse reflectance intensity and introduced an additional transition level at 2.8 eV, which corresponds well to the assumption that niobium creates shallow electron traps below the conduction band. Such an analysis of optical spectra of TiO_2:Nb is presented for the first time. Methylene blue, methyl orange and 4-chlorophenol were chosen as model molecules to investigate photocatalytic activity of TiO_2:Nb nanopowders under UVA and VIS irradiation in suspension type of reactor. TiO_2:Nb with Nb concentration up to 1 at.% showed good photocatalytic performance towards MB decomposition under both types of irradiation, better than commercial TiO_2-P25. MO could be decomposed only under UVA irradiation and TiO_2:0.1 at.% was the best performing material composition under this type of irradiation. 4-CP was decomposed only under UVA irradiation, and TiO_2:Nb nanopowders performed worse than TiO_2-P25. An improved photocatalytic performance of TiO_2:Nb is related to an improved light absorption in the visible range, Nb-related defect structure and higher surface acidity. Under VIS light irradiation, a degradation of MB was probably driven by photosensitized type of excitation. TiO_2:Nb is suggested as an efficient selective photocatalyst, which can be applied under solar irradiation because it showed an enhanced photocatalytic performance under UVA and VIS irradiation. However, due to the high photodegradation kinetic rates under UVA irradiation, the reaction is driven by the UVA part of the solar irradiation.

References

Akurati KK, Vital A, Dellemann J-P, Michalow K, Graule T, Ferri D, Baiker A (2008) Flame-made WO_3/TiO_2 nanoparticles: relation between surface acidity, structure and photocatalytic activity. Appl Catal, B 79:53–62

Almquist CB, Biswas P (2002) Role of synthesis method and particle size of nanostructured TiO_2 on its photoactivity. J Catal 212:145–156

Anukunprasert T, Saiwan C, Traversa E (2005) The development of gas sensor for carbon monoxide monitoring using nanostructure of Nb-TiO_2. Sci Technol Adv Mat 6:359–363

Asahi R, Morikawa T, Ohwaki T, Aoki K, Taga Y (2001) Visible-light photocatalysis in nitrogen-doped titanium oxides. Science 293:269–271

Atashbar MZ, Sun HT, Gong B, Wlodarski W, Lamb R (1998) XPS study of Nb-doped oxygen sensing TiO_2 thin films prepared by sol–gel method. Thin Solid Film 326:238–244

Awati PS, Awate SV, Shah PP, Ramaswamy V (2003) Photocatalytic decomposition of methylene blue using nanocrystalline anatase titania prepared by ultrasonic technique. Catal Commun 4:393–400

Borgarello E, Kiwi J, Grätzel M, Pellizetti E, Visca M (1982) Visible light induced water cleavage in colloidal solutions of chromium-doped titanium dioxide particles. J Am Chem Soc 104:2996–3002

Carotta MC, Ferroni M, Gnani D, Guidi V, Merli M, Martinelli G, Casale MC, Notaro M (1999) Nanostructured pure and Nb-doped TiO_2 as thick film gas sensors for environmental monitoring. Sens Actuators B 58:310–317

Chen X, Mao SS (2007) Titanium dioxide nanomaterials: synthesis, properties, modifications, and applications. Chem Rev 107:2891–2959

Cui H, Dwight K, Soled S, Wold A (1995) Surface acidity and photocatalytic activity of Nb_2O_5 photocatalysts. J Solid State Chem 115:187–191

Ferroni M, Carotta MC, Guidi V, Martinelli G, Ronconi F, Richard O, Van Dyck D, Van Landuyt J (2000) Structural characterization of Nb-TiO_2 nanosized thick-films for gas sensing application. Sens Actuators B 68:140–145

Finklea HO (1988) Semiconductor electrodes. Elsevier, Amsterdam, pp 58–61

Fox MA, Dulay MT (1993) Heterogeneous photocatalysis. Chem Rev 93:341–357

Fujishima A, Zhang X (2006) Titanium dioxide photocatalysis: present situation and future approaches. C R Chim 9:750–760

Gautron J, Lemasson P, Poumelec B, Marucco J-F (1983) Photoelectrochemical study of (Ti, V)O_2 and (Ti, Nb)O_2 alloys. Sol Energ Mater 9:101–111

Guillard C, Disdier J, Herrmann J-M, Lehaut C, Chopin T, Malato S, Blanco J (1999) Comparison of various titania samples of industrial origin in the solar photocatalytic detoxification of water containing 4-chlorophenol. Catal Today 54:217–228

Herrmann J-M, Matos J, Disdier J, Guillard C, Laine J, Malato S, Blanco J (1999) Solar photocatalytic degradation of 4-chlorophenol using the synergistic effect between titania and activated carbon in aqueous suspension. Catal Today 54:255–265

Hoffmann MR, Martin ST, Choi W, Bahnemann DW (1995) Environmental applications of semiconductor photocatalysis. Chem Rev 95:69–96

Houas A, Lachheb H, Ksibi M, Elaloui E, Guillard C, Herrmann J-M (2001) Photocatalytic degradation pathway of methylene blue in water. Appl Catal, B 31:145–157

Kubacka A, Colon G, Fernandez-Garcia M (2009) Cationic (V, Mo, Nb, W) doping of TiO_2-anatase: a real alternative for visible light-driven photocatalysts. Catal Today 143:286–292

Lakshmi S, Renganathan R, Fujita S (1995) Study on TiO_2-mediated photocatalytic degradation of methylene blue. J Photochem Photobiol A 88:163–167

Linsebigler AL, Guangquan L, Yates JT (1995) Photocatalysis on TiO_2 surface: principles, mechanism and selected results. Chem Rev 95:735–758

Mattsson A, Leideborg M, Larsson K, Westin G, Österlund L (2006) Adsorption and solar light decomposition of acetone on anatase TiO_2 and niobium doped TiO_2 thin films. J Phys Chem B 110:1210–1220

Messing GL, Zhang SC, Jayanthi GV (1993) Ceramic powder synthesis by spray pyrolysis. J Am Ceram Soc 76:2707–2726

Michalow K, Vital A, Heel A, Graule T, Reifler F, Ritter A, Zakrzewska K, Rekas M (2008) Photocatalytic activity of W-doped TiO_2 nanopowders. J Adv Oxid Technol 11:56–64

Michalow KA, Heel A, Vital A, Amberg M, Fortunato G, Kowalski K, Graule T, Rekas M (2009a) Effect of thermal treatment on the photocatalytic activity in visible light of TiO_2-W flame spray synthesized nanopowders. Top Catal 52:1051–1059

Michalow KA, Logvinovich D, Weidenkaff A, Amberg M, Fortunato G, Heel A, Graule T, Rekas M (2009b) Synthesis, characterization and electronic structure of nitrogen-doped TiO_2 nanopowder. Catal Today 144:7–12

Mills A, Davies R (1995) Activation energies in semiconductor photocatalysis for water purification: the 4-chlorophenol-TiO_2-O_2 photosystem. J Photochem Photobiol A 85:173–178

Mills A, Morris S (1993) Photomineralization of 4-chlorophenol sensitized by titanium dioxide: a study of the initial kinetics of carbon dioxide photogeneration. J Photochem Photobiol A 71:75–83

Mills A, Wang J (1999) Photobleaching of methylene blue sensitised by TiO_2: an ambiguous system? J Photochem Photobiol A 127:123–134

Mills A, Morris S, Davies R (1993) Photomineralization of 4-chlorophenol sensitized by titanium dioxide: a study of the intermediates. J Photochem Photobiol A 70:183–191

Mulmi DD, Sekiya T, Kamiya N, Kurita S, Murakami Y, Kodaira T (2004) Optical and electric properties of Nb-doped anatase TiO_2 single crystal. J Phys Chem Solid 65:1181–1185

Nowotny J, Bak T, Nowotny MK, Sheppard LR (2006) TiO_2 surface active sites for water splitting. J Phys Chem B 110:18492

Ogawa H, Abe A, Nishikawa M, Hayakawa S (1981) Preparation of tin oxide films from ultrafine particles. J Electrochem Soc 128:685–689

Ohtani B, Ogawa Y, Nishimoto S (1997) Photocatalytic activity of amorphous-anatase mixture of titanium(IV) oxide particles suspended in aqueous solutions. J Phys Chem B 101:3746–3752

Okazaki S, Okuyama T (1983) Nb_2O_5 supported on TiO_2. Catalytic activity for reduction of NO with NH_3. Bull Chem Soc Jpn 56:2159–2160

Onfroy T, Manoilova OV, Bukallah SB, Hercules DH, Clet G, Houalla M (2007) Surface structure and catalytic performance of niobium oxides supported on titania. Appl Catal A 316:184–190

Radecka M, Rekas M (1995) The studies of high-temperature interaction of Nb-TiO_2 thin films with oxygen. J Phys Chem Solid 56:1031–1037

Radecka M, Rekas M, Zakrzewska K (2006) Titanium dioxide in photoelectrolysis of water. Trends Inorg Chem 9:81–126

Radecka M, Rekas KE, Zakrzewska K, Heel A, Michalow KA, Graule T (2010) TiO_2-based nanopowders and thin films for photocatalytical application. J Nanosci Nanotechnol 10:1032–1042

Ruiz A, Dezanneau G, Arbiol J, Cornet A, Morante JR (2003) Study of the influence of Nb content and sintering temperature on TiO_2 sensing films. Thin Solid Film 436:90–94

Sclafani A, Herrmann J-M (1996) Comparison of photoelectronic and photocatalytic activities of various anatase and rutile forms of titania in pure liquid organic phases and in aqueous solutions. J Phys Chem 100:13655–13661

Shannon RD (1976) Revised effective ionic radii and systematic studies of interatomic distances in halides and chalcogenides. Acta Cryst A 32:751–767

Sharma RK, Bhatnagar MC, Sharma GL (1998) Mechanism in Nb doped titania oxygen gas sensor. Sens Actuators B 46:194–201

Sheppard L, Bak T, Nowotny J, Sorrell CC, Kumar S, Gerson AR, Barnes MC, Ball C (2006) Effect of niobium on the structure of titanium dioxide thin films. Thin Solid Film 510:119–124

Spurr RA, Myers H (1957) Quantitative analysis of anatase-rutile mixtures with an X-ray diffractometer. Anal Chem 29:760–762

Stone VF Jr, Davis RJ (1998) Synthesis, characterization, and photocatalytic activity of titania and niobia mesoporous molecular sieves. Chem Mater 10:1468–1474

Teleki A, Bjelobrk N, Pratsinis SE (2008) Flame-made Nb- and Cu-doped TiO_2 sensors for CO and ethanol. Sens Actuators B130:449–457

Tian G-L, He H-B, Shao J-D (2005) Effect of microstructure of TiO_2 thin film on optical band gap energy. Chin Phys Lett 22:1787–1789

Traversa E, Di Vona ML, Licoccia S, Sacerdoti M, Carotta MC, Crema L, Martinelli G (2001) Sol-gel processed TiO_2-based nano-sized powders for use in thick-film gas sensors for atmospheric pollutant monitoring. J Sol- Gel Sci Technol 22:167–179

Trenczek-Zajac A, Rekas M (2006) Electrical properties of Nb-doped titanium dioxide TiO_2 at room temperature. Mater Sci Poland 24:53–60

Trenczek-Zajac A, Radecka M, Rekas M (2007) Photoelectrochemical properties of Nb-doped titanium dioxide. Physica B 399:55–59

Trenczek-Zajac A, Radecka M, Jasinski M, Michalow KA, Rekas M, Kusior E, Zakrzewska K, Heel A, Graule T, Kowalski K (2009) Influence of Cr on structural and optical properties of TiO_2:Cr nanopowders prepared by flame spray synthesis (FSS). J Power Sources 194:104–111

Tsvetkov N, Larina L, Shevaleevskiy O, Tae Ahn B (2011a) Effect of Nb doping of TiO_2 electrode on charge transport in dye-sensitized solar cells. J Electrochem Soc 158:B1281–B1285

Tsvetkov N, Larina L, Shevaleevskiy O, Tae Ahn B (2011b) Electronic structure study of lightly Nb-doped TiO_2 electrode for dye-sensitized solar cells. Energ Environ Sci 4:1480–1486

Wang MH, Guo RJ, Tso TL, Perng TP (1995) Effects of sintering on the photoelectrochemical properties of Nb-doped TiO_2 electrodes. Int J Hydrogen Energy 20:555–560

Yan X, Ohno T, Abe R, Ohtani B (2006) Is methylene blue an appropriate substrate for a photocatalytic activity test? A study with visible-light responsive titania. Chem Phys Lett 429:606–610

Yang Y, Wu Q, Hu C, Wang E (2005) Efficient degradation of the dye pollutants on nonporous polyoxotungstate-anatase composite under visible-light irradiation. J Mol Catal A 225:203–212

Zaitsev SV, Moon J, Takagi H, Awano M (2000) Preparation and characterization of nanocrystalline doped TiO_2. Adv Powder Technol 11:211–220

Zakrzewska K, Radecka M, Rekas M (1997) Effect of Nb, Cr, Sn additions on gas sensing properties of TiO_2 thin films. Thin Solid Film 310:161–166